AGU PUBLICATIONS

JGR

Journal of Geophysical Research: Space Physics

RESEARCH ARTICLE
10.1002/2016JA023548

Key Points:
- First statistical study assessing the dynamic response of Mercury's magnetopause, bow shock, and northern cusp region to ICMEs
- During ICMEs, the magnetopause reaches Mercury's surface ~30% of the time and cusp plasma pressure is double that under average solar wind
- The ICME ram pressure and Alfvén Mach number are dominant factors affecting change in the magnetosphere; IMF also plays nonnegligible role

Supporting Information:
- Supporting Information S1
- Table S1

Correspondence to:
R. M. Winslow,
reka.winslow@unh.edu

Citation:
Winslow, R. M., L. Philpott, C. S. Paty, N. Lugaz, N. A. Schwadron, C. L. Johnson, and H. Korth (2017), Statistical study of ICME effects on Mercury's magnetospheric boundaries and northern cusp region from MESSENGER, *J. Geophys. Res. Space Physics*, *122*, 4960–4975, doi:10.1002/2016JA023548.

Received 1 OCT 2016
Accepted 4 APR 2017
Accepted article online 10 APR 2017
Published online 3 MAY 2017

Statistical study of ICME effects on Mercury's magnetospheric boundaries and northern cusp region from MESSENGER

Reka M. Winslow[1], Lydia Philpott[2], Carol S. Paty[3], Noé Lugaz[1], Nathan A. Schwadron[1], Catherine L. Johnson[2,4], and Haje Korth[5]

[1]Institute for the Study of Earth, Oceans, and Space, University of New Hampshire, Durham, New Hampshire, USA, [2]Department of Earth, Ocean and Atmospheric Sciences, University of British Columbia, Vancouver, British Columbia, Canada, [3]School of Earth and Atmospheric Sciences, Georgia Institute of Technology, Atlanta, Georgia, USA, [4]Planetary Science Institute, Tucson, Arizona, USA, [5]The Johns Hopkins University Applied Physics Laboratory, Laurel, Maryland, USA

Abstract This paper presents a systematic investigation of the large-scale processes in Mercury's magnetosphere during interplanetary coronal mass ejections (ICMEs) using observations from the MErcury Surface, Space ENvironment, GEochemistry, and Ranging (MESSENGER) mission. We study the motion of the bow shock and magnetopause boundaries, quantify the magnetospheric compression, and characterize the size, extent, and plasma pressure of the northern cusp region and the plasma precipitation to the surface. During ICMEs, the magnetopause was substantially compressed, as the subsolar standoff distance from the center of the planet was reduced by ~15% compared with the value during nominal solar wind conditions, and the magnetopause reached the surface of the planet ~30% of the time. On the other hand, the bow shock under ICME conditions was located farther from the planet than for nominal solar wind conditions. The cusp was observed to extend ~10° farther equatorward and 2 h wider in local time. In addition, the average plasma pressure in the cusp was more than double that determined under nominal conditions. For the most extreme cases, the particle precipitation to the surface was an order of magnitude higher than on average. The solar wind ram pressure and the Alfvén Mach number are found to be the dominant factors affecting these changes in the magnetosphere, with the interplanetary magnetic field (IMF) direction and the IMF magnetic pressure playing a small but likely nonnegligible role.

1. Introduction

The magnetosphere of Mercury is highly dynamic as a consequence of its close proximity to the Sun and Mercury's weak internal magnetic field [e.g., *Ness et al.*, 1974; *Slavin and Holzer*, 1979; *Slavin*, 2004; *Slavin et al.*, 2010; *Baker et al.*, 2016]. The dynamic nature of the magnetosphere is pushed to its extremes during times of interplanetary coronal mass ejections (ICMEs) [*Slavin et al.*, 2014]. The high frequency of ICMEs encountered during the MErcury Surface, Space ENvironment, GEochemistry, and Ranging's (MESSENGER's) 4 yearlong orbital mission [*Winslow et al.*, 2015] (in part due to Mercury's short orbital period and to the orbital mission coinciding with the recent solar maximum) allows for statistical studies of space weather effects on Mercury's magnetosphere.

At Earth, the effects of ICMEs on the magnetosphere have been studied for many decades [e.g., *Dungey*, 1961; *Smith et al.*, 1964; *Akasofu*, 1980; *Akasofu and Chao*, 1980]. Because ICMEs can be associated with strong southward interplanetary magnetic fields, high solar wind velocities, and enhanced solar wind ram pressures, they are strong drivers of geomagnetic storm activity at Earth [*Lindsay et al.*, 1995]. Geomagnetic storms are caused by the transfer of momentum and energy from the solar wind to the magnetosphere due to magnetic reconnection during times of southward interplanetary magnetic field. During geomagnetic storms, a large number of solar wind particles gain access to the magnetosphere, especially in the auroral regions, and cause the aurora to intensify and extend much farther in latitude than during quiescent conditions [*Baker*, 2000].

ICMEs, when they reach Earth, typically consist of a low-density, high-magnetic field, low-β (plasma thermal pressure to magnetic pressure ratio), low-Alfvén Mach number (M_A) magnetic ejecta, preceded by a dense sheath of high ram pressure. The effects of ICMEs on the magnetopause and bow shock boundaries at Earth

have been studied in great detail for several decades. Important parameters controlling these locations are the plasma β, the ram pressure, Mach number, and the strength of nonradial or north-south magnetic field [e.g., *Spreiter et al.*, 1966; *Zwan and Wolf*, 1976; *Shue et al.*, 1997, 1998]. The increased solar wind ram pressure associated with ICMEs as well as their fast speed can greatly compress the magnetosphere by moving the magnetopause closer to the planet [*Cho et al.*, 2010]. *Lavraud and Borovksy* [2008] predicted that due to the low Mach number nature of ICMEs, and especially magnetic clouds, asymmetric magnetosheath flows and asymmetric magnetopause shapes are expected. Low Mach number conditions also lead to the subsolar bow shock moving outward from the planet, as has been observed at the Earth [*Formisano et al.*, 1971; *Lugaz et al.*, 2016] and at Mercury [*Winslow et al.*, 2013].

Mercury has a weak internal field, described by a dipole moment 190 nT R_M^3 (where R_M is Mercury's radius), offset 0.2 R_M northward of the geographic equator and aligned with the rotation axis [*Anderson et al.*, 2011, 2012; *Johnson et al.*, 2012; *Winslow et al.*, 2014]. A statistical study by *Winslow et al.* [2013] showed that the magnetopause subsolar standoff distance is 1.45 R_M from the dipole origin, while the bow shock subsolar standoff distance is 1.96 R_M during average solar wind and interplanetary magnetic field (IMF) conditions. At Mercury's heliocentric distances, the solar wind density and ram pressure are an order of magnitude higher than at Earth. *Winslow et al.* [2013] found that to first order, the solar wind ram pressure controls the magnetopause position (magnetopause is closest to the planet for high pressure), while the Alfvén Mach number controls the bow shock location (boundary is closest to the planet for high Mach number). Other recent studies have looked in greater detail at the factors controlling Mercury's magnetosphere [e.g., *DiBraccio et al.*, 2013; *Gershman et al.*, 2015], including during extreme conditions [*Slavin et al.*, 2014], as well as the formation of plasma depletion layers (PDLs) in the magnetosheath [*Gershman et al.*, 2013] and the development of Kelvin-Helmholtz (KH) instability of Mercury's magnetopause [*Liljeblad et al.*, 2014; *Gershman et al.*, 2015].

Mercury's northern cusp region has been characterized under average solar wind conditions from MESSENGER observations [*Korth et al.*, 2011a; *Winslow et al.*, 2012; *Raines et al.*, 2014; *Poh et al.*, 2016]. The cusp has a mean latitudinal extent of ~11° (with a maximum observed range from 55.8°N to 83.6°N) and a mean local time extent of 4.5 h at MESSENGER altitudes. *Winslow et al.* [2012] estimated that $(1.1 \pm 0.6) \times 10^{24}$ protons s^{-1} from the solar wind bombard the cusp surface over an area of $(5.2 \pm 1.6) \times 10^{11}$ m^2. The Southern Hemisphere cusp region has not been observed because of MESSENGER's orbit; however, it has been predicted to be 4 times larger than its northern counterpart [*Anderson et al.*, 2011], and plasma precipitation to the surface there is expected to be correspondingly higher [*Winslow et al.*, 2012, 2014]. The northern cusp region of Mercury was also previously studied during three extreme events, two of which were selected ICME passages, by *Slavin et al.* [2014]. During these extreme solar wind conditions unusually deep diamagnetic depressions were observed in the cusp.

Work in the past decade on magnetic reconnection [e.g., *Cassak and Shay*, 2007, 2009], which drives much of Earth's and Mercury's magnetospheric dynamics and is largely responsible for supplying plasma to the cusps, has led to better understanding of reconnection at Earth's dayside magnetopause [e.g., *Borovsky et al.*, 2008; *Borovsky*, 2008; *Lopez et al.*, 2010]. At Earth, the reconnection rate is found to depend primarily on the solar wind Mach number, the plasma β, the ram pressure, and the magnetic field out-of-ecliptic angle. Studies of the reconnection rate at the dayside magnetopause of Mercury only started with the MESSENGER mission. These studies have revealed that dayside reconnection rate at the Hermean magnetopause is a factor of ~3 larger than at the Earth and is almost independent of the shear angle between the IMF and planetary field [*DiBraccio et al.*, 2013]. Reconnection at Mercury is primarily controlled by M_A [*DiBraccio et al.*, 2013; *Gershman et al.*, 2013] even during ICME passage [*Slavin et al.*, 2014]. The passage of ICMEs at Mercury is expected to result in low M_A, low plasma β, enhanced magnetic field strength, and enhanced north-south magnetic fields in the magnetic ejecta, as well as enhanced ram pressure in the sheath. The lower the M_A in the solar wind, the larger the scale of IMF magnetic flux pileup between the bow shock and the magnetopause that can give rise to a region of plasma depletion in the magnetosheath, called the plasma depletion layer (PDL). The low magnetopause plasma β that forms as a consequence of PDL formation has been observed to promote reconnection even for low shear angles at Mercury [*Gershman et al.*, 2013]. Reconnection is thus expected to proceed at an even faster rate during ICMEs at Mercury, regardless of the shear angle, which was shown to be the case during the two ICMEs studied by *Slavin et al.* [2014].

At Earth, the cusp plasma pressures and latitudinal extent of the cusp are controlled by the ram pressure of the solar wind and the reconnection rate [*Reiff et al.*, 1977; *Newell and Meng*, 1987; *Zhou et al.*, 2000].

Subsolar reconnection and reconnection at the antisunward boundary of Mercury's northern cusp inject plasma into the cusp region and enhance the diamagnetic depression associated with the cusp. Flux transfer events (FTEs), formed by reconnection at multiple X lines on the dayside magnetopause, have also been shown to be a significant source of plasma in Mercury's cusp region [*Slavin et al.*, 2014; *Poh et al.*, 2016]. High rates of reconnection at Mercury's magnetopause result in the formation of FTEs in rapid succession, termed FTE showers [*Slavin et al.*, 2012]. FTEs and FTE showers contribute to the cusp plasma filaments that have been observed in Mercury's northern cusp [*Poh et al.*, 2016].

As the magnetopause and bow shock boundaries, as well as the cusp region, are strongly affected by ICMEs at the Earth, it is of interest to statistically examine the effect of ICME passage on Mercury's already highly dynamic boundary region. At Mercury, ICMEs may be composed of relatively denser material as compared to at Earth, and the ram pressure may be enhanced throughout the ICME, potentially leading to stronger compression of the dayside magnetosphere. It has been hypothesized that due to mass loading of the magnetotail during extreme solar wind conditions, the dayside magnetopause may be entirely eroded at Mercury [*Slavin et al.*, 2010, 2014] giving the solar wind direct access to the planet's surface. This could lead to transient, enhanced space weathering and exosphere production at midlatitudes on the dayside of the planet. Magnetohydrodynamic [*Zurbuchen et al.*, 2004] and parametric [*Luhmann et al.*, 1998] models of Mercury's magnetosphere have also been applied during ICME events with similar results to that of *Slavin et al.* [2010]. The models predict magnetopause compression to the surface as well as a much larger area of open magnetic field lines. Compression of the magnetopause to or close to the surface is also predicted for a small percentage of the time under nonextreme solar wind conditions [*Johnson et al.*, 2016; *Zhong et al.*, 2015a, 2015b]. In this paper, we conduct a statistical study of Mercury's bow shock, magnetopause, and northern cusp under ICME conditions, and we quantify the magnetospheric compression and plasma precipitation to Mercury's surface during ICMEs.

2. Magnetospheric Boundaries

We selected all magnetospheric crossings that were affected by ICMEs at Mercury, using the ICME database in *Winslow et al.* [2015] and completing the database with events through to the end of the MESSENGER mission (see Table S1 in the supporting information) (note that *Winslow et al.* [2015] included ICMEs until October 2014, whereas the mission ended in April 2015). Sixty-nine ICMEs are included in this study, with a mean ICME magnetic field magnitude of ~55 nT, an average maximum field of ~93 nT, and a mean transit speed from Sun to Mercury of ~700 km/s for a mean Mercury heliocentric distance of 0.38 AU. Most ICMEs lasted longer than one MESSENGER orbit around Mercury (8 or 12 h, depending on the mission phase), and thus, multiple bow shock and magnetopause crossings were identified for these ICMEs. Therefore, the study includes 113 magnetospheric passages that were affected by ICMEs, and there is one average inbound and one average outbound boundary crossing for most magnetospheric passages. However, the number of bow shock crossings (221) and magnetopause crossings (225) included in the data set were not even, due to the fact that we only included in the analysis magnetospheric boundary crossings that occurred after the ICME arrival. This meant that in a few cases the inbound magnetospheric boundaries were not included due to the ICME's arrival after the start of the magnetospheric crossing. There were also a few cases where the bow shock was not observed, which accounts for the unequal number of bow shock and magnetopause crossings.

We used the same identification and analysis methods as in *Winslow et al.* [2013] for Mercury's bow shock and magnetopause. For boundary identification, the same philosophy was applied: because multiple boundary crossings may be observed for each magnetospheric passage as a result of the motion of the boundary relative to the spacecraft, we identified the times of the innermost and outermost crossing on each pass for the bow shock and the magnetopause. This method provides demarcations for the inner and outer limits of the boundaries, within and outside of which the spacecraft was in the magnetosphere, magnetosheath, or in the interplanetary medium (i.e., ICME).

2.1. Average Boundaries

In order to characterize the average bow shock and magnetopause shapes and locations under ICME conditions, we fit empirical model curves to the boundary locations. As in *Winslow et al.* [2013], the boundary locations were specified with two different techniques: (1) by finding the midpoint of the inner and outer boundary limits on each magnetospheric pass and (2) by establishing a probability density map of the boundary to determine the locations of maximum residence probability for the boundary. For the latter, we

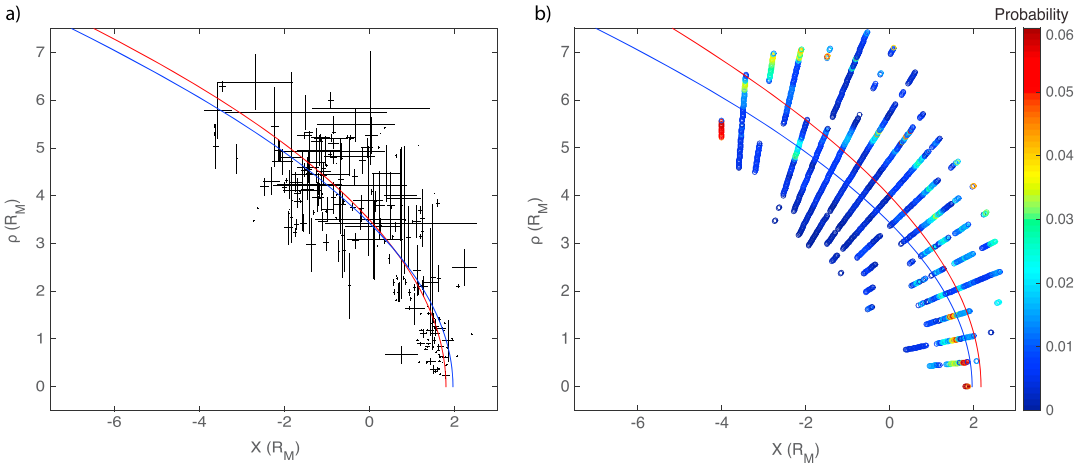

Figure 1. (a) Midpoints between the inner and outer aberrated bow shock crossing positions identified from MESSENGER Magnetometer data during ICME conditions. Error bars show the distance between the inner and outer crossings. Curves show the best fit conic section to the data (red) given by $p = 3.4\ R_M$, $\epsilon = 1.0$, and $X_0 = 0.1\ R_M$ and the best fit conic section from *Winslow et al.* [2013] to the bow shock under average solar wind conditions (blue). (b) Probability density map of binned aberrated bow shock positions during ICME conditions. The blue regions represent areas where the bow shock is very rarely observed and the dark red regions where it is observed most often. The red curve represents the conic section that best fits the probability densities presented here given by $p = 3.5\ R_M$, $\epsilon = 1.03$, and $X_0 = 0.4$, while the blue curve represents the best fit conic section from *Winslow et al.* [2013] to the probability densities under average solar wind conditions. The probabilities sum to 1 along each θ bin.

registered the spacecraft trajectories between each inner and outer crossing limits on spatial grids around the planet, and the number of crossings passing through each grid cell was used to build a probability density map of the region of space in which the boundaries were most likely to be encountered (see details in *Winslow et al.* [2013]). Empirical shapes were then fit to both the boundary midpoints and the probability density maps, with the established probabilities used as weights in the fitting for the latter. Due to the accumulated data in the probability density maps, we regard the fit to the probability densities to be a more accurate representation of the average boundary. In the figures that follow, all boundary locations are in aberrated Mercury solar magnetic (MSM) coordinates, where the X axis is directed from Mercury's offset magnetic dipole toward the center of the Sun, the Z axis is normal to Mercury's orbital plane toward the north celestial pole, and the Y axis completes the right-handed system with the positive direction oriented opposite to the orbital motion. For the offset of the magnetic dipole from the center of Mercury along the Z axis, we used a value of 0.198 R_M to reflect the average offset found for the entire MESSENGER mission duration. The aberration correction was calculated from the planet's instantaneous orbital speed together with an average solar wind speed of 700 km s^{-1}, i.e., our average estimated ICME speed at Mercury. The ρ coordinate is defined as $\rho = \sqrt{Y^2 + Z^2}$. In addition, we have assumed that the boundaries are figures of revolution about the line through the dipole center that parallels the X axis. Although *Zhong et al.* [2015a] showed that the magnetopause is well fit by an asymmetric model that includes a cusp indentation, it is not possible to confirm this asymmetry from our limited, ICME-affected boundary data set.

Figures 1 and 2 show the bow shock and magnetopause locations under ICME conditions, respectively. These figures show that the overall shape of these boundaries is not drastically different under ICME conditions compared with nominal solar wind conditions. Thus, the same empirical shapes that were used to fit the boundaries in *Winslow et al.* [2013] still apply here. In that paper, the best fit model to the bow shock was found to be a conic section given by

$$\sqrt{(X - X_0)^2 + \rho^2} = \frac{p\epsilon}{1 + \epsilon \cdot \cos\theta}, \tag{1}$$

where X_0 is the focus point, ϵ is the eccentricity, p is the focal parameter, and $\theta = \tan^{-1}\left(\frac{\rho}{X}\right)$. For the magnetopause, the best fit empirical shape was given by the model of *Shue et al.* [1997] (hereafter referred to as the Shue et al. model):

$$R = \sqrt{X^2 + \rho^2} = R_{ss}\left(\frac{2}{1 + \cos\theta}\right)^{\alpha}, \tag{2}$$

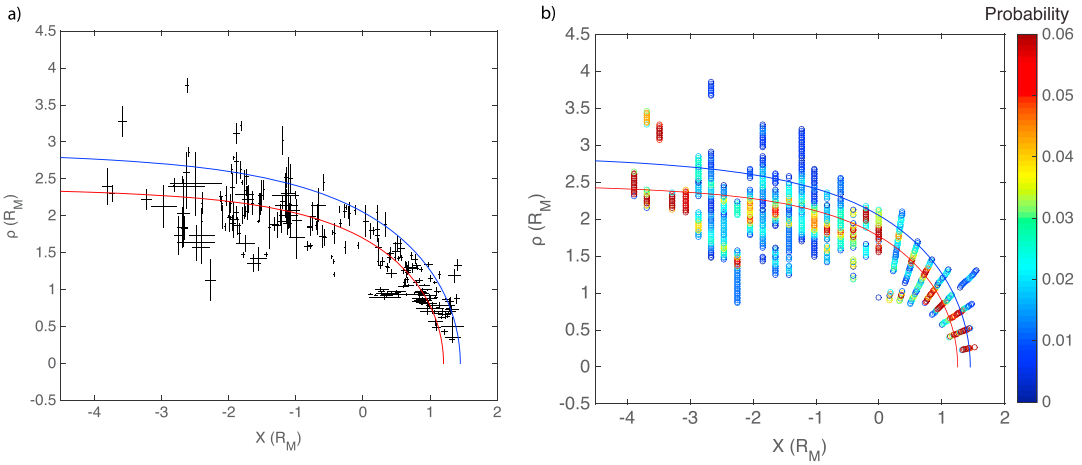

Figure 2. (a) Midpoints between the inner and outer aberrated magnetopause crossing positions. Curves show the best fit Shue et al. model to the data (red) given by $R_{ss} = 1.2\,R_M$ and $\alpha = 0.5$, and the best fit Shue et al. model from *Winslow et al.* [2013] to the magnetopause under average solar wind conditions (blue). (b) Probability density map of the aberrated magnetopause crossings. The red curve represents the Shue et al. model that best fits the probability densities presented here given by $R_{ss} = 1.25\,R_M$ and $\alpha = 0.5$, while the blue curve represents the best fit Shue et al. model from *Winslow et al.* [2013] to the probability densities under average solar wind conditions. The probabilities sum to 1 along each X bin on the nightside and along each θ bin on the dayside.

where R is the distance from the dipole center and α is the flaring parameter that governs how open the magnetotail is. We used these models to fit to our ICME-affected bow shock and magnetopause crossing locations, using a grid search method that minimized the root-mean-square (RMS) residual of the perpendicular distance of the observed midpoints from the model boundary.

Here for times during ICME passage, we found that for the bow shock the best fit conic section to the midpoint locations is given by $p = 3.4\,R_M$, $\epsilon = 1.0$, and $X_0 = 0.1\,R_M$, resulting in a nose distance of 1.80 R_M. Our best fit model has an RMS misfit of ~1500 km (0.64 R_M) between model boundary and bow shock position. For the probability density maps, a conic fit to the grid cell locations weighted by the probabilities yielded slightly different model parameters, given by $p = 3.5\,R_M$, $\epsilon = 1.03$, and X_0=0.4, resulting in a nose distance of 2.18 R_M, and with a reduced RMS misfit of 215 km (0.09 R_M) that reflects the use of the probabilities as weights. In comparison, the best fit subsolar standoff distance under nominal solar wind was found to be 1.90 R_M for the midpoint fits and 1.96 R_M for the probabilistic fits by *Winslow et al.* [2013]. For the magnetopause, the best fit Shue model curve is given by $R_{ss} = 1.2\,R_M$ and $\alpha = 0.5$ and RMS misfit of 777 km (0.32 R_M) for the midpoint fit, while for the probability density map the best fit curve is $R_{ss} = 1.25\,R_M$ and α=0.5, with a weighted RMS misfit of 151 km (0.06 R_M). *Winslow et al.* [2013] found $R_{ss} = 1.45\,R_M$ for both midpoint and probabilistic fits during nominal solar wind conditions. As mentioned above, it is possible that Mercury's magnetopause includes a cusp indentation not captured by our symmetric Shue et al. model fit. With this data set we are not able to discriminate between a magnetopause crossing close to the planet due to a cusp indentation and one due to a highly compressed symmetric magnetopause shape. To ensure that crossings possibly within a cusp indentation do not unduly influence our best fit magnetopause shape, we conducted a midpoint and a probabilistic fit excluding magnetopause crossings where MESSENGER crosses the boundary very close to the cusp region (specifically category 2 and a subset of category 3 cusp cases described in section 3.1 below). In the case of the midpoint fit, the best fit model to the magnetopause excluding the "near-cusp" points yielded $R_{ss} = 1.3\,R_M$ and $\alpha = 0.45$, with only a 4 km difference in RMS misfit when compared to the fit of $R_{ss} = 1.2\,R_M$ and $\alpha = 0.5$ for the same data set. In the case of the probabilistic fit, the resulting best fit R_{ss} and α were unchanged.

The results from our analysis during ICME passage (red curves) and those of *Winslow et al.* [2013] under nominal solar wind (blue curves) are plotted in Figures 1 and 2. For the bow shock, the ICME-affected best fit curve is closer to the planet at the nose of the shock but is farther from the planet at high ρ for the midpoint fit, as compared with the curves established under average solar wind, while it is everywhere farther from the planet in the case of the probabilistic fit. The difference in subsolar standoff distance between nominal and ICME conditions is a 5% decrease in the case of the midpoint fit and an 11% increase in the case of the

probabilistic fit, from the center of the dipole, while at a high ρ of 5 R_M there is a 2% increase in the distance from the dipole center for the midpoint fit and a 5% increase for the probabilistic fit. In the case of the magnetopause, the boundary is found closer to the planetary surface during ICME conditions than during nominal solar wind (with a subsolar standoff distance decrease of 14–17% from the dipole origin). The increase in the average bow shock standoff distance coupled with the decrease in magnetopause standoff distance results in 33–82% increase in the magnetosheath size at Mercury during ICME passage, with a range of 0.60–0.93 R_M (with the range reflecting results from midpoint or probabilistic fits).

2.2. Effects of Ram Pressure and Alfvén Mach Number

To quantitatively test the boundaries' response to extreme solar wind conditions, we calculate proxies of P_{Ram} and M_A using MESSENGER Magnetometer data. Given that MESSENGER did not directly measure the solar wind density and the solar wind velocity could only be derived about 50% of the time that MESSENGER was in the solar wind [*Gershman et al.*, 2012], and because there was no upstream solar wind monitor, the derived proxies below are the only self-consistent estimates that we can use to constrain the solar wind conditions during our observed boundary crossings. For each magnetospheric transit where an ICME has been identified, we determined a proxy for the solar wind ram pressure from the magnetopause magnetic field strength. During nominal solar wind conditions, the magnetopause is in pressure balance between two dominant components, the solar wind ram pressure and the magnetic pressure of the planet's magnetosphere. We assumed a Newtonian approximation and equated the magnetic pressure of the magnetosphere, $P_{B_{\mathrm{sph}}}$, to P_{Ram} through

$$P_{B_{\mathrm{sph}}} = KP_{\mathrm{Ram}} \cos^2 \psi, \tag{3}$$

where K is a constant and ψ is the angle between the magnetopause normal and the upstream solar wind direction. The parameter K determines how much the ram pressure has been diminished by the divergence of the flow due to the obstacle of the planet's magnetic field. The gas dynamic result for this parameter is $K = 0.88$ [*Kivelson and Russell*, 1995], and we adopted this value in this study.

For the purposes of this study, however, the assumption that the pressure balance is only between the solar wind ram pressure and the planet's magnetic pressure is likely not always accurate. In order to improve on our P_{Ram} proxy, we take into account the IMF magnetic field strength, which in rare cases can be as high as the magnetospheric field at times of magnetic ejecta passage. Also, at times when MESSENGER observes the cusp near the magnetopause crossing, we included the magnetospheric thermal plasma pressure into the pressure balance. The new pressure balance is then given by

$$0.88P_{\mathrm{Ram}} \cos^2 \psi + P_{B_{\mathrm{IMF}}} = P_{Th_{\mathrm{sph}}} + P_{B_{\mathrm{sph}}}, \tag{4}$$

where $P_{B_{\mathrm{IMF}}}$ is the IMF magnetic pressure and $P_{Th_{\mathrm{sph}}}$ is the thermal pressure of the magnetosphere near the magnetopause due to plasma present in the cusp.

In order to estimate P_{Ram} from our observations, we used 30 mins averages of the IMF magnitude upstream of the outermost bow shock crossing to calculate $P_{B_{\mathrm{IMF}}}$. $P_{B_{\mathrm{sph}}}$ was determined from the average of the highest 20% of B values in 1 min just inside of the innermost magnetopause to avoid including diamagnetic depressions. $P_{Th_{\mathrm{sph}}}$ was estimated from the average cusp plasma pressure in cases where the cusp was near the magnetopause (see section 3 below for more details). To estimate the angle, ψ, between the magnetopause normal direction and the solar wind velocity, we first applied an abberation correction to the positions of the innermost magnetopause crossings. We then assumed a Shue et al. magnetopause shape with a flaring of $\alpha = 0.5$, passing through any given innermost magnetopause crossing and determined the normal direction to the Shue et al. magnetopause shape at that point. ψ was then the angle between this normal and the aberrated X_{MSM} direction. We note that this method for estimating P_{Ram} can only be used for dayside observations and is unreliable at large ψ because there the thermal pressure that was converted from ram pressure cannot be neglected. We thus only estimate a P_{Ram} proxy for magnetopause crossings where $\psi < 60°$, and we also excluded one additional outlier point with $\psi = 59.8°$ that had an unrealistically large P_{Ram} value of 488 nPa.

We then also used the P_{Ram} proxy to estimate a proxy for M_A, since M_A can be expressed as

$$M_A = \frac{v_{\mathrm{sw}}}{v_A} = \frac{\sqrt{\mu_0 P_{\mathrm{Ram}}}}{B_{\mathrm{IMF}}}, \tag{5}$$

where v_{sw} is the solar wind flow speed, v_A is the Alfvén speed, and μ_0 is the permeability of free space.

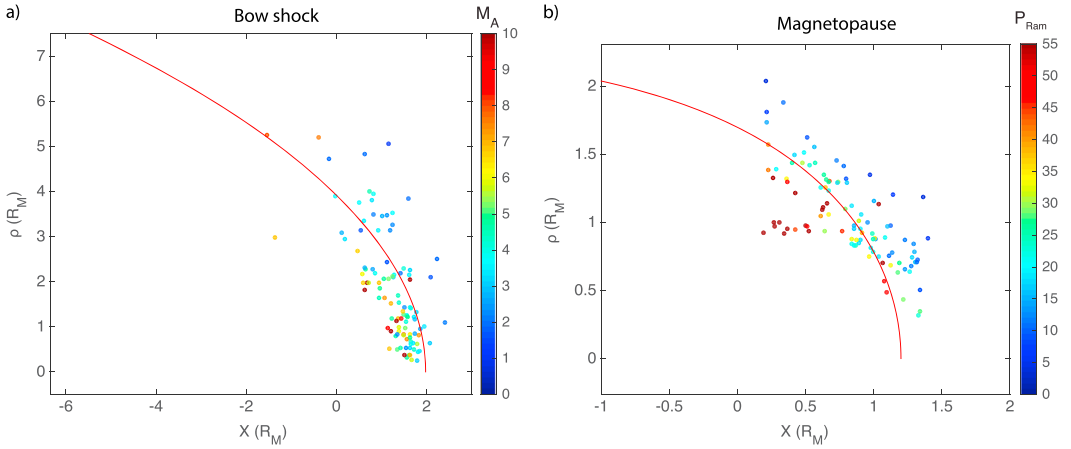

Figure 3. (a) Midpoints of the bow shock crossings color coded by solar wind Alfvén Mach number. The solid red curve through the data is the conic section best fit to the midpoints shown in Figure 1a. (b) Midpoints of the magnetopause crossings color coded by solar wind ram pressure. The solid red curve through these data points is the best fit Shue et al. model as shown in Figure 2a.

Figure 3 shows the bow shock and magnetopause locations for which we can derive M_A and P_{Ram} proxies, color coded by the corresponding proxies. There are 104 magnetopause crossings for which we can estimate P_{Ram} out of 225 ICME-affected magnetopause crossings in the data set. This means that for most orbits, we can estimate P_{Ram} for either the inbound or the outbound crossings, so that at least one P_{Ram} value can be assigned for nearly all magnetospheric crossings. For the bow shock, the highest M_A crossings are closest to the planet on average; the points that fall inside the best fit bow shock boundary have an average M_A of 5.6, while the average M_A is 3.5 for the points outside the boundary (Figure 3a). The increase in the average bow shock distance from the planet during ICMEs is due to the lower Alfvén Mach number expected during the passage of magnetic ejecta. Similarly, Figure 3b shows that the magnetopause is closest to the planet for the highest values of P_{Ram}. Thus, the decrease in the average magnetopause distance from the planet during ICMEs is due to the ram pressure increase expected during ICMEs.

Flaring of Mercury's magnetopause is expected to occur in addition to the change of the subsolar distance of the bow shock and magnetopause. The main drivers of the flaring are thought to be variation in the ram pressure, Mach number, and plasma β during the passage of ICMEs. The magnetopause flaring will be different depending on the part of the ICME affecting the magnetosphere and the intensity of the dayside compression, which may result in very high or very low flaring during an ICME passage. In addition, Mercury's magnetosphere responds quickly to any change in the solar wind conditions, making it impossible to know the actual solar wind conditions during a magnetotail crossing. With the relatively small number of events, it is not possible to separate the different effects and to determine the flaring of the magnetosphere under different conditions. We find that the average flaring remains at $\alpha = 0.5$ during ICMEs, same as during average solar wind conditions. As can be seen in Figure 2a, there are a large number of points with a very compressed tail, consistent with strong dayside compression and small-to-average flaring. There are also a few points with a highly flared magnetotail, consistent with magnetic flux loading of the tail. In addition, under strong northward interplanetary magnetic field that is expected to be common inside ICMEs, KH instabilities are known to form in the duskside of the magnetosphere [*Paral and Rankin*, 2013; *Gershman et al.*, 2015], which could also have an influence on the flaring of the magnetopause. With the limited statistics available in this study and the lack of upstream solar wind monitor at Mercury, it is impossible to perform a more advanced investigation of the flaring of Mercury's magnetosphere during ICME passage.

For average solar wind conditions, the study by *Winslow et al.* [2013] determined that the subsolar magnetosheath thickness was 0.51 R_M. In this study, we found that the subsolar thickness is 0.93 R_M (using probability density map) or 0.6 R_M (using midpoints). The increase is partly due to the retreat of the magnetopause and partly to the sunward motion of the bow shock. As such, low Mach numbers and high ram pressures during ICMEs are important factors affecting the sheath thickness. However, it is important to note that PDLs may occupy a significant fraction of the magnetosheath during low Mach number conditions, potentially up to 20% of the entire thickness [*Gershman et al.*, 2013], which is especially pertinent during ICMEs.

We also note that there are two ICME cases when no bow shock was observed at Mercury, i.e., either the bow shock was farther upstream of the planet than MESSENGER's orbit or temporarily no bow shock formed due to sub-Alfvénic conditions. These occurred on 25 May 2012 and on 20–21 August 2013, at which time our M_A proxy was ~2 for both cases. This indicates a low M_A; however, it does not suggest sub-Alfvénic conditions, which likely exemplifies the limitations of our M_A proxy. The proxy can be used as a relative indicator of high and low M_A; however, it is likely not accurate enough to determine the absolute value for individual cases (similarly, the same is true of P_{Ram}).

2.3. Compression of the Dayside Magnetosphere to the Surface

Assuming a Shue et al. model shape of Mercury's magnetopause, with the best fit flaring parameter of $\alpha = 0.5$, we can estimate how often the magnetopause reaches the planetary surface during ICMEs. Mercury's offset dipole means that the symmetric magnetopause shape given by the Shue et al. model intersects the planet's surface when $R_{ss} < 1.05\ R_M$ for $\alpha = 0.5$. We fit Shue et al. model curves for each magnetopause crossing using the fixed flaring parameter mentioned and calculated an R_{ss} value for each crossing. We find that the magnetopause reaches the surface of the planet on 29% of the ICME-affected orbits (using the innermost magnetopause boundary crossing). Using the same criteria, *Johnson et al.* [2016] found that on average (for the entire MESSENGER mission), the percentage of time the magnetopause is below the surface is 4%. To place bounds on our estimate, we also calculated the percentage of ICME-affected orbits when the magnetopause is below the surface for a 20% increase and decrease in the magnetopause flaring parameter α. For $\alpha = 0.4$, the magnetopause is below the surface in 15% of orbits, while for $\alpha = 0.6$, it is below the surface in 49% of orbits. This shows that the results are sensitive to the magnetopause flaring; however, due to the nature of MESSENGER's orbit and changes in solar wind conditions during each orbit, the flaring cannot be accurately established for each orbit individually. We note, however, that on average, Mercury's magnetopause is best fit by $\alpha = 0.5$ for both ICME and nominal solar wind conditions, suggesting that when taken over a large number of events over time, this value is most appropriate. The values given here for the percentage of time the magnetopause is below the surface, based on a symmetric Shue et al. model, may overestimate the true values if Mercury's magnetopause has an indentation in the cusp region. Excluding magnetopause crossings where MESSENGER crosses the boundary very close to the cusp (as discussed above in section 2.1), we find that the magnetopause reaches the surface of the planet on 25% of the orbits for $\alpha = 0.5$. This is a relatively small decrease as compared to the 29% found when including all magnetopause crossings.

The fact that approximately in one in three ICME-affected orbits the magnetopause reaches the planetary surface and leaves it exposed to the interplanetary medium, is largely due to the high ram pressure associated with ICMEs. The average magnetopause shape in *Winslow et al.* [2013] was derived under a mean ram pressure of 14.3 nPa, while in this study, the mean P_{Ram} was estimated to be 36.4 nPa. Furthermore, for the cases of $R_{ss} < 1.05\ R_M$, the mean ram pressure was found to be 86 nPa, which is substantially higher than the value for the entire data set. As determined in *Winslow et al.* [2013] and confirmed in this study, the ram pressure exerts a dominant influence on the magnetopause boundary location, with the highest P_{Ram} moving the boundary closest to the planet.

3. Cusp

3.1. Cusp Observations

Building on the study of *Winslow et al.* [2012], we identified and characterized Mercury's northern hemispheric cusp region during ICME-affected orbits. The cusp was identified from both 1 s total field data and from residuals of this measured total field after the subtraction of the state-of-the-art magnetospheric model field for Mercury [*Korth et al.*, 2015]. We visually selected the cusp as distinct depressions in the field (both in the measured and residual fields) larger than ~30 nT that were at least 2–3 min in duration and that occurred when the spacecraft was passing over high northern latitudes on the dayside (or close to the terminator). The residual observations allowed for easier identification, especially in cases of shallow diamagnetic depressions. Through this identification process, we split the cusp into four different categories: (1) The cusp was clearly observed and was far from either the inbound or outbound magnetopause crossings (Figure 4a) (61 cases)—we refer to these cases as "typical cusp"; (2) the cusp was clearly observed, but it was very close to the magnetopause boundary (Figure 4b) (15 cases)—we refer to these cases as "cusp near magnetopause"; (3) the cusp was not clearly observed either due to the proximity of the magnetopause or due to MESSENGER's orbit being in a dawn-dusk configuration, although some cusp signatures were present in some of the cases (Figure 5a)

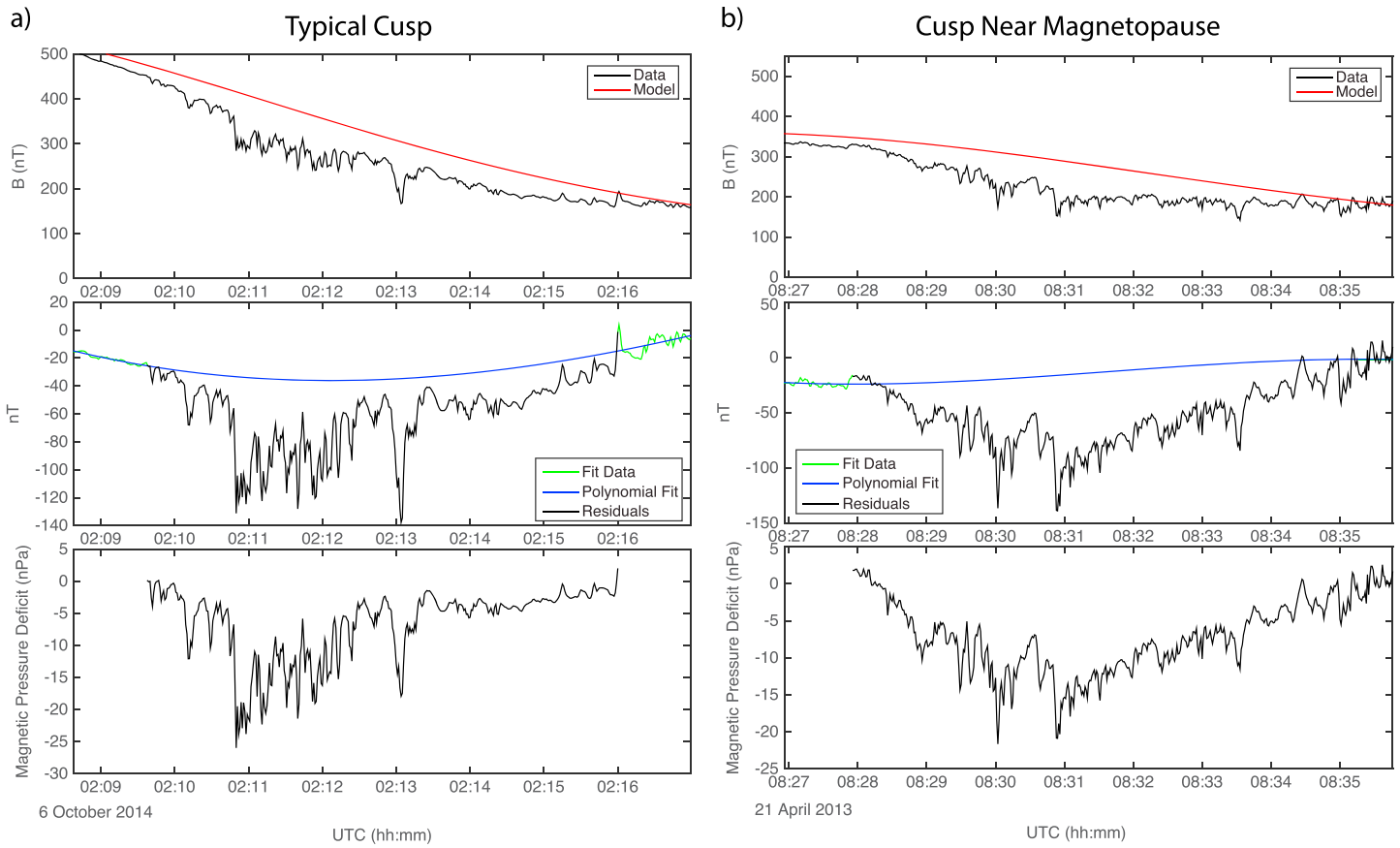

Figure 4. Example cusp observations for (a) a "typical" ICME cusp case (category 1) and (b) a "cusp near the magnetopause" case (category 2). (top) Measured (black) and modeled (red) magnetic field magnitude in the cusp region. (middle) Magnetic depression in the residual $|B|$ (black), residual data before and after cusp (green), and a third-degree polynomial fit (blue) to the green curve. (bottom) The calculated pressure deficit ($-P_{\text{Plasma}}$). In Figure 4b, there is no residual data (green curve) after the cusp due to the magnetopause encounter; thus, data averaged within 1 min of the cusp ending are used for the polynomial fit.

(27 cases); and (4) there was clearly no cusp observed (Figure 5b) (10 cases). Figures 4 and 5 show representative cusp examples for each category.

The latter two categories were used to distinguish between cases where a cusp may have been present but MESSENGER did not observe all of it due to observational limitations (category 3) versus cases where there was no detectable cusp at all and this was not due to an observational limitation (category 4). Cases that were deemed category 4 were ones where the cusp region was not expected to be near the observed magnetopause crossing; the expected latitude and longitude range of the cusp was clearly observed in the magnetometer data, and no diamagnetic depression of significant depth or duration was detected.

3.2. Plasma Pressure in the Cusp

For each of categories 1 and 2 cusp observations, we inferred a plasma pressure from the magnetic field observations. Here we briefly summarize the plasma pressure calculation, and for more details the reader is referred to *Winslow et al.* [2012]. We calculated the plasma pressure that balances the magnetic field depression observed in the cusp region from $P_{\text{Total}} = P_{\text{Total}} + P_{\text{Plasma}}$, where P_{Total} is the total pressure; P_{Mag} is the magnetic pressure, $B^2/(2\mu_0)$; and P_{Plasma} is the particle thermal pressure. We estimated P_{Total} from the unperturbed magnetic field, B_U, in the cusp which was determined by adding the magnetospheric model field to a third-degree polynomial fit to the residuals ~1 min before and after but excluding the depression region (Figure 4, middle). We then evaluated $P_{\text{Total}} = B_U^2/(2\mu_0)$ and the magnetic pressure deficit $P_{B-deficit} = P_{\text{Mag}} - P_{\text{Total}} = -P_{\text{Plasma}}$ (Figure 4, bottom). This magnetic pressure deficit is an additional plasma pressure in the cusp relative to any background plasma pressure in the magnetosphere, although spot checks of observations by MESSENGER's Fast Imaging Plasma Spectrometer (FIPS) for a selection of orbits do not show substantial proton counts adjacent to but outside the cusp region for category 1 typical cusps.

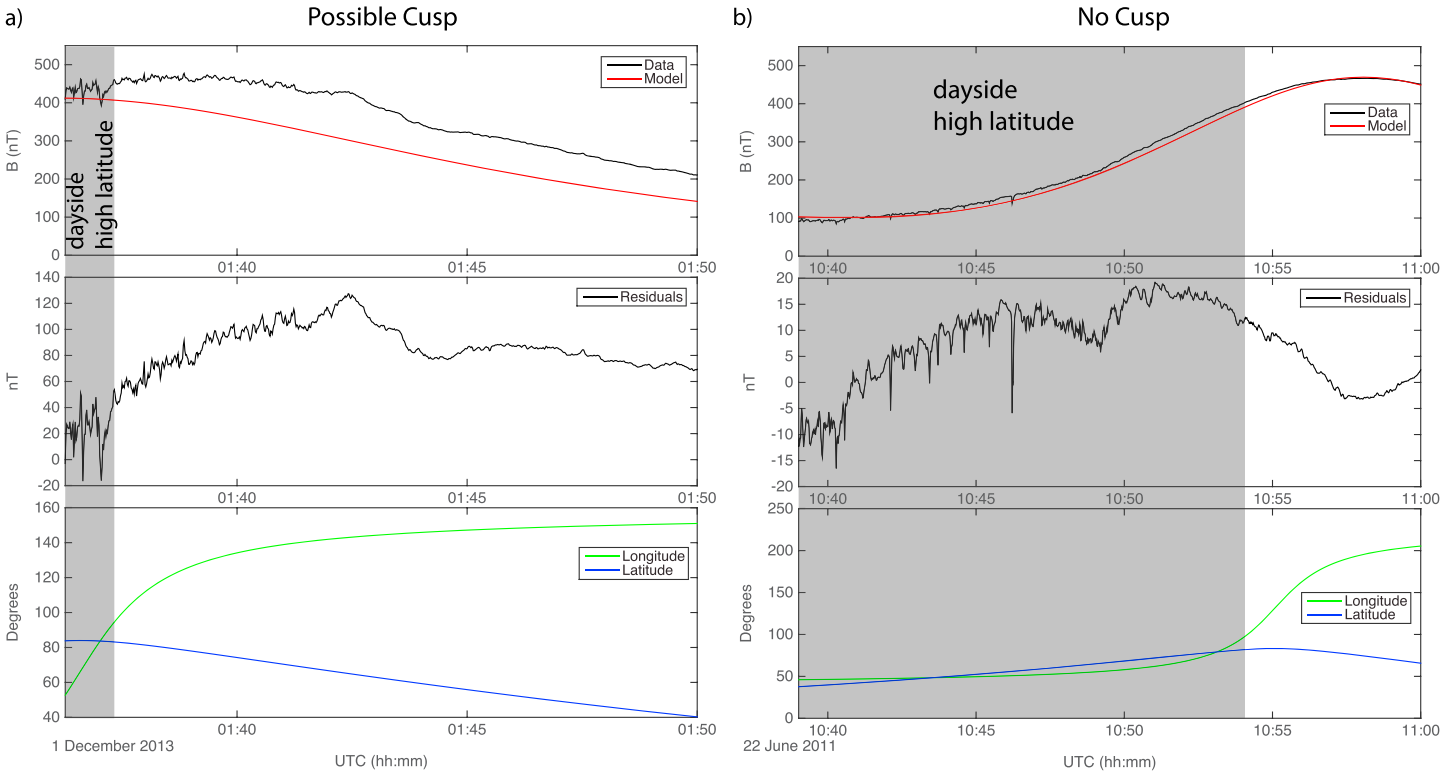

Figure 5. Example cusp observations for (a) a "possible cusp" case (category 3) and (b) a "no cusp" case (category 4). (top) Measured (black) and modeled (red) magnetic field magnitude in the cusp region. (middle) Residual magnetic field observations. (bottom) MESSENGER's latitude and longitude in degrees. Grey shaded regions indicate high-latitude dayside areas where the cusp is expected.

The magnetic pressure deficit (and thus the plasma pressure) was evaluated at each 1 s data point during MESSENGER's passage through the cusp. Figure 6 shows stereographic projection plots of the spacecraft trajectory through all ICME-affected cusp crossings, color coded by the magnetic pressure deficit. The data are shown in aberrated Mercury Solar Orbital (MSO) coordinate system in these figures. In MSO coordinates, X_{MSO} is positive sunward, Z_{MSO} is positive northward, Y_{MSO} is positive duskward and completes the right-handed system, and the origin is at the center of the planet. The cusp is observed to have a mean latitudinal extent of 19.6° centered on ~70°N MSO latitude, with maximal limits between 84.0°N and 46.0°N, where the lowest-latitude

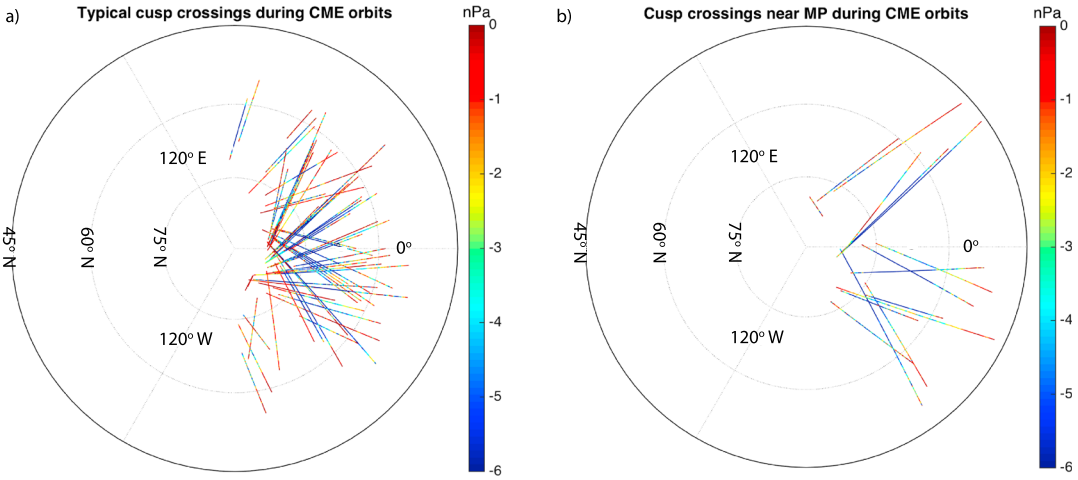

Figure 6. Stereographic projections of the aberrated spacecraft trajectory through the cusp, color coded by the magnetic pressure deficit ($-P_{Plasma}$) in the cusp. (a) Typical cusp cases. (b) Cusp cases near the magnetopause. The color bar is saturated so that observed, but localized, pressure deficits greater in magnitude than 6 nPa are shown in dark blue.

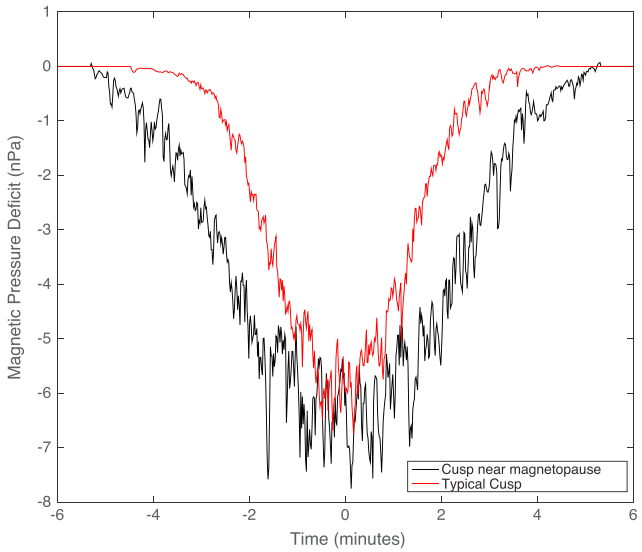

Figure 7. Superposed epoch analysis of the magnetic pressure deficit in the cusp for the typical cusp cases (red) and for the cusp cases near the magnetopause (black).

crossings correspond to cases where the cusp was observed near the magnetopause. The cusp is observed at nearly all local times on the dayside of the planet under ICME conditions, although the highest-plasma density is observed within ~3 h of noon. In comparison, the limits of the cusp under nominal solar wind conditions were found to be 55.8°N to 83.6°N and 7.2 to 15.9 h local time in *Winslow et al.* [2012], with a mean cusp extent of 11° centered on ~72°N.

To derive an average magnetic depression signature under ICME conditions, we conducted a superposed epoch analysis of the magnetic pressure deficit in the cusp for all cusp crossings in categories 1 and 2, separately (Figure 7). The average maximum plasma pressure from the superposed epoch analysis (or correspondingly, the average depth of the magnetic pressure deficit) of ~7 nPa in the cusp for ICME-affected orbits is more than double that observed under nominal solar wind conditions in *Winslow et al.* [2012]. The cusp is also generally more extended in time (reflected in the greater latitude extent found above).

3.3. Flux of Particles to the Surface

We can also estimate the flux of plasma to the surface under ICME conditions, from the derived plasma pressure at the spacecraft altitude. We followed the method laid out in *Winslow et al.* [2012] and in *Winslow et al.* [2014]. We assumed an isotropic and gyrotropic particle distribution entering from the magnetosheath. We first derived an expression for the plasma pressure ratio between the spacecraft and the surface, used it to calculate the surface pressure, and from there calculated the particle flux to the surface. By Liouville's theorem, the downgoing phase-space density of particles is preserved along the field line. The measured magnetic pressure deficit is due to the pressure from particle motions perpendicular to the local field direction, and thus, we can calculate the ratio between the pressure due to the downgoing particles at the surface, P_s, and the perpendicular pressure at the spacecraft altitude, $P_{\perp 0}$, in the absence of electric fields parallel to B. The surface acts as a sink for particles, which affects the pressure ratio by depleting the upgoing population. The magnetic field strength at the spacecraft altitude and the estimate of the surface field strength allowed us to estimate the pressure ratio under the assumption that pitch angles that mirror below the surface are lost from the upgoing portion of the phase-space density. From the mean B in the cusp region at spacecraft altitude during ICME conditions, and assuming perfect reflection, we found that $P_s/P_{\perp 0} = 0.75$, and for perfect absorption we found $P_s/P_{\perp 0} = 0.78$. Together with the mean P_{Plasma} (or $P_{\perp 0}$) of 4.5 nPa during cusp crossings, this yields a mean surface pressure of $P_s = 3.5 \pm 0.1$ nPa, where the uncertainty corresponds to the mean standard error on the pressure ratio multiplied by the mean surface pressure. We also estimate a mean surface pressure for the maximum P_{Plasma} measured in the cusp during ICMEs of 46.9 nPa, which yields a surface pressure of $P_s = 35.9 \pm 0.7$ nP, where the uncertainty is half the difference in the surface pressure between the upper and lower limits (as defined by perfect absorption and perfect reflection), as a standard error cannot be evaluated for one measurement point.

For an isotropic gas, the flux of particles through a surface is given by $\Phi = P/\sqrt{2\pi mkT}$, where m is the particle mass, T is the temperature, and k is Boltzmann's constant. To estimate the flux of particles to the surface, the surface pressure, P_s, was doubled to account for the upgoing half of the distribution. We assumed that the plasma is dominated by protons, and we used a characteristic energy of particles in the cusp of ~1.0 keV from FIPS observations. These assumptions yield a mean surface flux of $(6.4 \pm 2.9) \times 10^{12}$ particles $\mathrm{m}^{-2}\mathrm{s}^{-1}$ and a maximum surface flux during ICME conditions of $(6.6 \pm 3.0) \times 10^{13}$ particles $\mathrm{m}^{-2}\mathrm{s}^{-1}$. The mean surface flux obtained here is a factor of ~3 higher than the average proton flux to the surface in the Northern Hemisphere

Table 1. Means and Standard Deviations of the Maximum Cusp Plasma Pressure Along Each Cusp Crossing, Under Different Sign of the IMF Component

	$+B_X$	$-B_X$	$+B_Y$	$-B_Y$	$+B_Z$	$-B_Z$
Mean(P_{Plasma}) (nPa)	16.0	16.1	15.7	16.5	12.7	18.3
SD(P_{Plasma}) (nPa)	8.8	8.7	10.0	6.9	7.6	8.7

estimated by *Winslow et al.* [2012] using the same method, and the maximum calculated surface flux during ICMEs is more than an order of magnitude higher than the average value under nominal solar wind conditions.

3.4. Effects of External Conditions on the Cusp

We analyzed various factors affecting the cusp plasma pressure, to determine the dominant driver. We first assessed whether the ICME section (i.e., ICME sheath versus magnetic ejecta (ME)) had an influence on the plasma pressure in the cusp. Out of 76 cusp observations (categories 1 + 2), only 7 occurred during the ICME sheath passage. A further six categories 1 and 2 cusp crossings occurred during an ICME where there was no distinguishable ME section, i.e., the magnetic field was highly variable throughout the ICME passage. The low number of cusp observations during ICME sheath passage is partly due to the short time duration of the ICME sheath as compared to the ME duration and also due to the way the ICMEs were identified in the MESSENGER data. Our selection of ICMEs required the observation of the ICME shock/sheath arrival, i.e., MESSENGER had to be outside of the magnetosphere at the time of the shock arrival for the ICME to be recorded in our database; thus, the sheath passage was well before the magnetosphere (and therefore the cusp) encounter for most cases. Due to the low statistics, we cannot draw any conclusions about how the ICME sheath might affect the cusp differently from the ME. However, this analysis did reveal that despite the fact that most of our cusp observations occur during the ME passage, the variation in cusp plasma pressure is very large (from close to 0 nPa for category 4 to ~30 nPa for the deepest cusp crossings). Thus, significantly different conditions must exist during the different ME passages.

It was shown in *Korth et al.* [2011b] and *Winslow et al.* [2012, 2013] that under nominal solar wind conditions at Mercury's heliocentric distances, the IMF B_Y and B_Z components change sign on the timescale of minutes, thereby rendering the MESSENGER data not suitable for studying IMF B_Y and B_Z effects on Mercury's cusp region. However, in the ME the magnetic field varies slowly, on the timescale of hours, therefore allowing us to analyze IMF effects on the cusp under ICME conditions. Using data from only ME passages, we used 30 min averages of the magnetic field outside of the outermost bow shock closest in time to the cusp to establish the approximate IMF direction at the time of the cusp crossing. We then evaluated whether the IMF direction had a noticeable influence on the plasma pressure in the cusp. We first determined the maximum cusp plasma pressure along each crossing and then determined the average of these for positive and negative IMF B_X, B_Y, and B_Z. The results of these are shown in Table 1, along with the standard deviations. The mean cusp plasma pressures are quite similar under positive and negative IMF B_X and B_Y, while for negative IMF B_Z the plasma pressure is increased by ~6 nPa as compared to positive B_Z. It should be noted that given the high value of the standard deviation, this is not a statistically significant result. Without more observations, we cannot ascertain in a statistically significant manner whether the IMF B_Z direction is affecting Mercury's cusp plasma pressure. We also note that *Winslow et al.* [2012] observed a slight, but statistically significant, IMF B_X effect on the cusp plasma pressure, with increased P_{Plasma} for negative as compared to positive IMF B_X. A negative IMF B_X is expected to facilitate plasma transport into the northern cusp [*Kallio and Janhunen*, 2003]; however, such an effect is not observed in this study.

However, this study establishes that the dominant driver affecting the plasma pressure in the cusp is likely to be the solar wind ram pressure. Since the cusp is a region where plasma and magnetic pressures are similar, small changes in the solar wind ram pressure can have a significant effect on the cusp [*Zong et al.*, 2008]. Figure 8 shows P_{Plasma} versus P_{Ram} for typical cusp cases (category 1) and cusp cases that are near the magnetopause (category 2), with a robust linear regression fit to the data that highlights that there is a trend in the data of increasing P_{Plasma} with increased P_{Ram}. To determine if P_{Plasma} is linearly dependent on P_{Ram}, we calculated the Pearson correlation coefficient, which was found to be $r = 0.56$, with one significant outlier (P_{Ram}=213 nPa) removed from the calculation. We also assessed the correlation coefficients separately for categories 1 and 2 cusp cases and found a correlation coefficient of $r = 0.54$ for category 1 and a coefficient of $r = 0.76$ for category 2 cases. The low number of points with P_{Ram} >55 nPa in Figure 8 brings into question

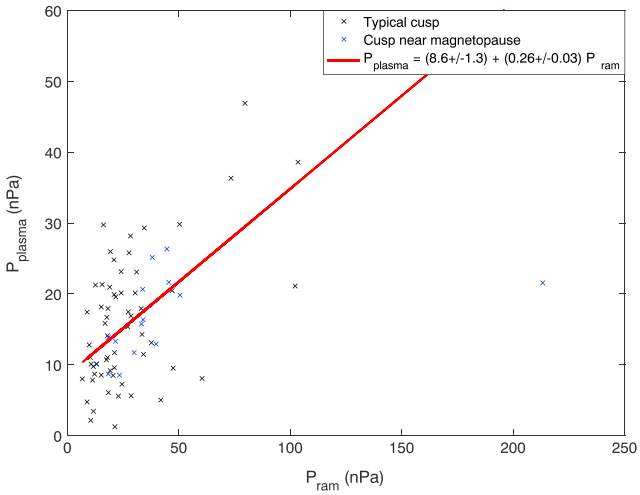

Figure 8. Maximum plasma pressure in the cusp as a function of the estimated ram pressure for category 1 (typical cusp cases) and category 2 (cusp cases near the magnetopause) cusp cases. A robust linear regression fit to the data is also shown.

the robustness of the calculated correlation. To show that there is still a correlation regardless of these points, albeit weaker, we removed points with the largest P_{Ram} ($P_{\mathrm{Ram}} > 55$ nPa) and found the correlation coefficient to be $r = 0.39$. Overall, there is a moderate positive correlation between P_{Plasma} in the cusp and solar wind P_{Ram}, accounting for some of the variation of cusp plasma pressure with ICMEs.

The increased magnetic field strength in MEs compared with nominal IMF conditions results in a stronger than average magnetic pressure exerted on the magnetosphere during ICMEs (as discussed in section 2.2 above). We therefore investigated whether the IMF magnetic pressure, $P_{B_{\mathrm{IMF}}}$, has a discernible effect on the cusp plasma pressure, P_{Plasma}. The Pearson correlation coefficient between $P_{B_{\mathrm{IMF}}}$ and P_{Plasma} was found to be 0.26, suggesting the possibility of IMF magnetic pressure influence. Given the stronger influence of the ram pressure, P_{Ram}, on the cusp, it is necessary to separate out the effect of the IMF magnetic pressure. We removed the P_{Ram} effect by multiplying P_{Plasma} by P_{Ram_0}/P_{Ram_i}, where P_{Ram_0} represents the mean P_{Ram} and P_{Ram_i} is the ith point in the series under evaluation. After applying this normalization, we recalculated the Pearson correlation coefficient between the normalized cusp plasma pressure and IMF magnetic pressure. The new correlation coefficient, r, was found to be −0.04, indicating essentially no correlation. Overall, similar to the magnetic field direction in the ME, the magnetic pressure may play a role in modulating the cusp plasma pressure at Mercury; however, this signal is not strong enough to separate from the influence of other ICME parameters in the data.

Due to the expected increase in the magnetic reconnection rate during low M_A conditions at Mercury, we assessed whether we could detect any M_A influence on P_{Plasma} in the cusp. Similar to the IMF magnetic pressure analysis above, no clear correlation between M_A and cusp plasma pressure was found in our data.

We also compared the P_{Ram} values for cases of no cusp observations (category 4) to cusp observations (categories 1 + 2). The median P_{Ram} was 12.4 nPa for cases where no cusp was observed, and it was 21.7 nPa for the cusp observations, hinting at possible P_{Ram} influence. However, there is a very large variance in P_{Ram} for both cases, with a standard deviation of 45.6 nPa for no cusp cases and 28.6 nPa for cusp cases. This suggests that variation in P_{Ram} is likely not the only significant factor affecting plasma pressure in the cusp. Furthermore, due to the small number of observations, the analysis of IMF effects on the no cusp observations was not revealing. Future detailed case studies of these category 4 cusp crossings may be able to shed some light on why some ICMEs induce high plasma densities and pressures in Mercury's cusp, while others do not induce any significant cusp plasma pressures.

4. Conclusions

Using orbital MESSENGER Magnetometer observations between March 2011 and April 2015, we have characterized Mercury's magnetospheric boundaries and northern cusp region during extreme solar wind conditions resulting from the passage of ICMEs. We determined the average empirical shape of the bow shock and the magnetopause and found that similar to *Winslow et al.* [2013], the bow shock is well fit by a hyperboloid of revolution, while the magnetopause is well fit by the Shue et al. model shape. However, the bow shock is on average between 2 and 11% farther from the dipole center, while the magnetopause is 14–17% closer to the dipole origin than under nominal solar wind conditions. Using a solar wind ram pressure proxy and Alfvén Mach number proxy that we established on an orbit-by-orbit basis from the magnetopause location, we determined that an increase in ram pressure and decrease in M_A during ICMEs are responsible for the motion of

these boundaries compared to average conditions. The assumption of a Shue et al. magnetopause shape with a flaring parameter of $\alpha = 0.5$ yields the estimate that Mercury's magnetopause reaches the planet's surface ~30% of the time during ICMEs, leaving Mercury's regolith directly exposed to the shocked solar wind at these times. Over time, such exposure can increase space weathering of the surface.

We have also for the first time provided a detailed analysis of the size, extent, and plasma pressure of Mercury's northern cusp in response to ICMEs. We found that on average, the cusp extends ~10° farther south, is 2 h wider in local time, and the average maximum plasma pressure in the cusp is a factor of 2 higher than under nominal solar wind conditions. Furthermore, we estimated a mean flux of particles to the surface of $(6.4 \pm 2.9) \times 10^{12}$ particles $m^{-2}s^{-1}$ and a maximum surface flux during ICME conditions of $(6.6 \pm 3.0) \times 10^{13}$ particles $m^{-2}s^{-1}$, which is an order of magnitude higher than under nominal solar wind. A moderate positive correlation was observed between the solar wind ram pressure and the cusp plasma pressure, while an IMF B_Z effect on the plasma pressure was also noted but this was found to be not statistically significant. Observations from the upcoming BepiColombo mission should shed further light on this result and potentially make it possible to separate IMF effects from solar wind effects on Mercury's cusp region.

The availability of 4 years of magnetometer observations from the MESSENGER spacecraft in orbit around Mercury has allowed us to statistically assess the dynamic response of Mercury's magnetosphere to strong ICME drivers. Space weather effects on Earth's magnetosphere have been studied for many decades; however, due to a lack of observations, such studies have so far not been feasible at other planets in our solar system. This study yields insight into the response of a small magnetosphere close to the Sun to extreme solar wind drivers and opens the door to comparative planetology studies of space weather effects on magnetospheres in the solar system.

Acknowledgments
Support for this work was provided by NASA grant NNX15AW31G. R.M.W. and C.P. are supported by NASA grant NNX15AW31G, and R.M.W. is supported by NSF grant AGS1622352. N.L. acknowledges support from NASA grant NNX15AB87G and NSF grant AGS1433213. N.A.S. acknowledges support from NASA grants NNG11PA03C, NNX07AC14G, NNX07AC14G, and NNX13AC89G and NSF grants AGS1135432 and AGS1622352. C.L.J. and L.P. acknowledge support from the Natural Sciences and Engineering Research Council (NSERC) of Canada. MESSENGER data are available on the Planetary Data System (https://pds.jpl.nasa.gov).

References

Anderson, B. J., C. L. Johnson, H. Korth, M. E. Purucker, R. M. Winslow, J. A. Slavin, S. C. Solomon, R. L. McNutt, J. M. Raines, and T. H. Zurbuchen (2011), The global magnetic field of Mercury from MESSENGER orbital observations, *Science*, *333*, 1859–1862, doi:10.1126/science.1211001.

Anderson, B. J., C. L. Johnson, H. Korth, R. M. Winslow, J. E. Borovsky, M. E. Purucker, J. A. Slavin, S. C. Solomon, M. T. Zuber, and R. L. McNutt Jr. (2012), Low-degree structure in Mercury's planetary magnetic field, *J. Geophys. Res.*, *117*, E00L12, doi:10.1029/2012JE004159.

Akasofu, S.-I. (1980), Study of individual geomagnetic storms in terms of the solar wind, *Planet. Space Sci.*, *28*, 933–944, doi:10.1016/0032-0633(80)90065-3.

Akasofu, S.-I., and J. K. Chao (1980), Interplanetary shock waves and magnetospheric substorms, *Planet. Space Sci.*, *28*, 381–385, doi:10.1016/0032-0633(80)90042-2.

Baker, D. N. (2000), Effects of the Sun on the Earth's environment, *J. Atmos. Sol. Terr. Phys.*, *62*, 1669, doi:10.1016/S1364-6826(00)00119-X.

Baker, D. N., et al. (2016), Intense energetic electron flux enhancements in Mercury's magnetosphere: An integrated view with high-resolution observations from MESSENGER, *J. Geophys. Res. Space Physics*, *121*, 2171–2184, doi:10.1002/2015JA021778.

Borovsky, J. E. (2008), The rudiments of a theory of solar wind/magnetosphere coupling derived from first principles, *J. Geophys. Res. Space Physics*, *113*, A08228, doi:10.1029/2007JA012646.

Borovsky, J. E., M. Hesse, J. Birn, and M. Kuznetsova (2008), What determines the reconnection rate at the dayside magnetosphere, *J. Geophys. Res. Space Physics*, *113*, A07210, doi:10.1029/2007JA012645.

Cassak, P. A., and M. A. Shay (2007), Scaling of asymmetric magnetic reconnection: General theory and collisional simulations, *Phys. Plasmas*, *14*, 102114, doi:10.1063/1.2795630.

Cassak, P. A., and M. A. Shay (2009), Structure of the dissipation region in fluid simulations of asymmetric magnetic reconnection, *Phys. Plasmas*, *16*, 55704, doi:10.1063/1.3086867.

Cho, K.-S., S.-C. Bong, Y.-J. Moon, M. Dryer, S.-E. Lee, and K.-H. Kim (2010), An empirical relationship between coronal mass ejection initial speed and solar wind dynamic pressure, *J. Geophys. Res.*, *115*, A10111, doi:10.1029/2009JA015139.

DiBraccio, G. A., J. A. Slavin, S. A. Boardson, B. J. Anderson, H. Korth, T. H. Zurbuchen, J. M. Raines, D. N. Baker, R. L. McNutt Jr., and S. C. Solomon (2013), MESSENGER observations of magnetopause structure and dynamics at Mercury, *J. Geophys. Res. Space Physics*, *118*, 997–1008, doi:10.1002/jgra.50123.

Dungey, J. W. (1961), Interplanetary magnetic field and the auroral zones, *Phys. Rev. Lett.*, *6*, 47–48, doi:10.1103/PhysRevLett.6.47.

Formisano, V., P. C. Hedgecock, G. Moreno, J. Sear, and D. Bollea (1971), Observations of Earth's bow shock for low Mach numbers, *Planet. Space Sci.*, *19*, 1519–1531, doi:10.1016/0032-0633(71)90011-0.

Gershman, D. J., et al. (2012), Solar wind alpha particles and heavy ions in the inner heliosphere observed with MESSENGER, *J. Geophys. Res.*, *117*, A00M02, doi:10.1029/2012JA017829.

Gershman, D. J., J. A. Slavin, J. M. Raines, T. J. Zurbuchen, B. J. Anderson, H. Korth, D. N. Baker, and S. C. Solomon (2013), Magnetic flux pileup and plasma depletion in Mercury's subsolar magnetosheath, *J. Geophys. Res. Space Physics*, *118*, 7181–7199, doi:10.1002/2013JA019244.

Gershman, D. J., et al. (2015), MESSENGER observations of solar energetic electrons within Mercury's magnetosphere, *J. Geophys. Res. Space Physics*, *120*, 8559–8571, doi:10.1002/2015JA021610.

Gershman, D. J., J. M. Raines, J. A. Slavin, T. H. Zurbuchen, T. Sundberg, S. A. Boardson, B. J. Anderson, H. Korth, and S. C. Solomon (2015), MESSENGER observations of multiscale Kelvin-Helmholtz vortices at Mercury, *J. Geophys. Res. Space Physics*, *120*, 4354–4368, doi:10.1002/2014JA020903.

Johnson, C. L., et al. (2012), MESSENGER observations of Mercury's magnetic field structure, *J. Geophys. Res.*, *117*, E00L14, doi:10.1029/2012JE004217.

Johnson, C. L., L. C. Philpott, B. J. Anderson, H. Korth, S. A. Hauck, D. Heyner II, R. J. Phillips, R. M. Winslow, and S. C. Solomon (2016), MESSENGER observations of induced magnetic fields in Mercury's core, *Geophys. Res. Lett.*, *43*, 2436–2444, doi:10.1002/2015GL067370.

Kallio, E., and P. Janhunen (2003), Solar wind and magnetospheric ion impact on Mercury's surface, *Geophys. Res. Lett.*, *30*(17), 1877, doi:10.1029/2003gl017842.
Kivelson, M. G., and C. T. Russell (1995), *Introduction to Space Physics*, Cambridge Univ. Press, Cambridge, U. K.
Korth, H., B. J. Anderson, J. M. Raines, J. A. Slavin, T. H. Zurbuchen, C. L. Johnson, M. E. Purucker, R. M. Winslow, S. C. Solomon, and R. L. McNutt Jr. (2011a), Plasma pressure in Mercury's equatorial magnetosphere derived from MESSENGER Magnetometer observations, *Geophys. Res. Lett.*, *38*, L22201, doi:10.1029/2011GL049451.
Korth, H., et al. (2011b), The interplanetary magnetic field environment at Mercury's orbit, *Planet. Space Sci.*, *59*, 2075–2085, doi:10.1016/j.pss.2010.10.014.
Korth, H., N. A. Tsyganenko, C. L. Johnson, L. C. Philpott, B. J. Anderson, M. M. Al Asad, S. C. Solomon, and R. L. McNutt Jr. (2015), Modular model for Mercury's magnetospheric magnetic field confined within the average observed magnetopause, *J. Geophys. Res. Space Physics*, *120*, 4503–4518, doi:10.1002/2015JA021022.
Lavraud, B., and J. E. Borovksy (2008), Altered solar wind-magnetosphere interaction at low Mach numbers: Coronal mass ejections, *J. Geophys. Res.*, *113*, A00B08, doi:10.1029/2008JA013192.
Liljeblad, E., T. Sundberg, T. Karlsson, and A. Kullen (2014), Statistical investigation of Kelvin-Helmholtz waves at the magnetopause of Mercury, *J. Geophys. Res. Space Physics*, *119*, 9670–9683, doi:10.1002/2014JA020614.
Lindsay, G. M., C. T. Russell, and J. G. Luhmann (1995), Coronal mass ejection and stream interaction region characteristics and their potential geomagnetic effectiveness, *J. Geophys. Res.*, *100*, 16,999–17,013.
Lopez, R. E., R. Bruntz, E. J. Mitchell, M. Wiltberger, J. G. Lyon, and V. G. Merkin (2010), Role of magnetosheath force balance in regulating the dayside reconnection potential, *J. Geophys. Res.*, *115*, A12216, doi:10.1029/2009JA014597.
Lugaz, N., C. J. Farrugia, C.-L. Huang, R. M. Winslow, H. Spence, and N. A. Schwadron (2016), Earth's magnetosphere and outer radiation belt under sub-Alfvénic solar wind, *Nat. Commun.*, *7*, 13001, doi:10.1038/ncomms13001.
Luhmann, J. G., C. T. Russell, and N. A. Tsyganenko (1998), Disturbances in Mercury's magnetosphere: Are the Mariner 10 substorms simply driven, *J. Geophys. Res.*, *103*, 9113–9120, doi:10.1029/97JA03667.
Ness, N. F., K. W. Behannon, R. P. Lepping, Y. C. Whang, and K. H. Schatten (1974), Magnetic field observations near Mercury: Preliminary results from mariner 10, *Science*, *185*, 151–160, doi:10.1126/science.185.4146.151.
Newell, P. T., C.-I. Meng (1987), Cusp width and Bz: Observations and a conceptual model, *J. Geophys. Res.*, *92*(A12), 13,673–13,678, doi:10.1029/JA092iA12p13673.
Paral, J., and R. Rankin (2013), Dawn-dusk asymmetry in the Kelvin-Helmholtz instability at Mercury, *Nat. Commun.*, 1645, doi:10.1038/ncomms2676.
Poh, G., J. A. Slavin, X. Jia, G. A. DiBraccio, J. M. Raines, S. M. Imber, D. J. Gershman, W-J. Sun, B. J. Anderson, H. Korth, T. H. Zurbuchen, R. L. McNutt Jr., and S. C. Solomon (2016), MESSENGER observations of cusp plasma filaments at Mercury, *J. Geophys. Res. Space Physics*, 8260–8285, doi:10.1002/2016JA022552.
Raines, J. M., D. J. Gershman, J. A. Slavin, T. H. Zurbuchen, H. Korth, B. J. Anderson, and S. C. Solomon (2014), Structure and dynamics of Mercury's magnetospheric cusp: MESSENGER measurements of protons and planetary ions, *J. Geophys. Res. Space Physics*, *119*, 6587–6602, doi:10.1002/2014JA020120.
Reiff, P. H., T. W. Hill, J. L. Burch (1977), Solar wind plasma injection at the dayside magnetospheric cusp, *J. Geophys. Res.*, *82*(4), 479–491, doi:10.1029/JA082i004p00479.
Shue, J.-H., J. K. Chao, H. C. Fu, C. T. Russell, P. Song, K. K. Khurana, and H. J. Singer (1997), A new functional form to study the solar wind control of the magnetopause size and shape, *J. Geophys. Res.*, *102*, 9497–9511, doi:10.1029/97JA00196.
Shue, J.-H., P. Song, C. T. Russell, J. T. Steinberg, J. K. Chao, G. Gastenker, O. L. Vaisberg, S. Kokubun, H. J. Singer, T. R. Detman, and H. Kawano (1998), Magnetopause location under extreme solar wind conditions, *J. Geophys. Res*, *103*(A8), 17,691–17,700, doi:10.1029/98JA01103.
Slavin, J. A., and R. E. Holzer (1979), The effect of erosion on the solar wind stand-off distance at Mercury, *J. Geophys. Res.*, *84*, 2076–2082, doi:10.1029/JA084iA05p02076.
Slavin, J. A. (2004), Mercury's magnetosphere, *Adv. Space Res.*, *33*, 1859–1874, doi:10.1016/j.asr.2003.02.019.
Slavin, J. A., et al. (2010), MESSENGER observations of extreme loading and unloading of Mercury's magnetic tail, *Science*, *329*, 665–668, doi:10.1126/science.1188067.
Slavin, J. A., et al. (2012), MESSENGER observations of a flux-transfer-event shower at Mercury, *J. Geophys. Res.*, *117*, A00M06, doi:10.1029/2012JA017926.
Slavin, J. A., et al. (2014), MESSENGER observations of Mercury's dayside magnetosphere under extreme solar wind conditions, *J. Geophys. Res. Space Physics*, *119*, 8087–8116, doi:10.1002/2014JA020319.
Smith, E. J., C. P. Sonett, and J. W. Dungey (1964), Satellite observations of the geomagnetic field during magnetic storms, *J. Geophys. Res.*, *69*, 2669–2688, doi:10.1029/JZ069i013p02669.
Spreiter, J. R., A. L. Summers, and A. Y. Alksne (1966), Hydromagnetic flow around the magnetosphere, *Planet. Space Sci.*, *14*, 223–253, doi:10.1016/0032-0633(66)90124-3.
Winslow, R. M., C. L. Johnson, B. J. Anderson, H. Korth, J. A. Slavin, M. E. Purucker, and S. C. Solomon (2012), Observations of Mercury's northern cusp region with MESSENGER's Magnetometer, *Geophys. Res. Lett.*, *39*, L08112, doi:10.1029/2012GL051472.
Winslow, R. M., B. J. Anderson, C. L. Johnson, J. A. Slavin, H. Korth, M. E. Purucker, D. N. Baker, and S. C. Solomon (2013), Mercury's magnetopause and bow shock from MESSENGER Magnetometer observations, *J. Geophys. Res. Space Physics*, *118*, 2213–2227, doi:10.1002/jgra.50237.
Winslow, R. M. (2014), Investigation of Mercury's magnetospheric and surface magnetic fields, PhD thesis, The University of British Columbia, Vancouver, B. C.
Winslow, R. M., C. L. Johnson, B. J. Anderson, D. J. Gershman, J. M. Raines, R. J. Lillis, H. Korth, J. A. Slavin, S. C. Solomon, T. H. Zurbuchen, and M. T. Zuber (2014), Mercury's surface magnetic field determined from proton-reflection magnetometry, *Geophys. Res. Lett.*, 4463–4470, doi:10.1002/2014GL060258.
Winslow, R. M., N. Lugaz, L. C. Philpott, N. A. Schwadron, C. J. Farrugia, B. J. Anderson, and C. W. Smith (2015), Interplanetary coronal mass ejections from MESSENGER orbital observations at Mercury, *J. Geophys. Res. Space Physics*, 6101–6118, doi:10.1002/2015JA021200.
Zhong, J., W. X. Wan, J. A. Slavin, Y. Wei, R. L. Lin, L. H. Chai, J. M. Raines, Z. J. Rong, and X. H. Han (2015a), Mercury's three-dimensional asymmetric magnetopause, *J. Geophys. Res. Space Physics*, 7658–7671, doi:10.1002/2015JA021425.
Zhong, J., W. X. Wan, Y. Wei, J. A. Slavin, J. M. Raines, Z. J. Rong, L. H. Chai, and X. H. Han (2015b), Compressibility of Mercury's dayside magnetopause, *Geophys. Res. Lett.*, *42*, 10,135–10,139, doi:10.1002/2015GL067063.
Zhou, X. W., C. T. Russell, G. Le, S. A. Fuselier, J. D. Scudder (2000), Solar wind control of the polar cusp at high altitude, *J. Geophys. Res.*, *105*(A1), 245–251, doi:10.1029/1999JA900412.

Zong, Q.-G., et al. (2008), Multiple cusps during an extended northward IMF period with a significant B_y component, *J. Geophys. Res.*, *113*, A01210, doi:10.1029/2006JA012188.

Zurbuchen, T. H., P. Koehn, L. A. Fisk, T. Gombosi, G. Gloeckler, and K. Kabin (2004), On the space environment of Mercury, *Adv. Space Res.*, *33*, 1884–1889, doi:10.1016/j.asr.2003.04.048.

Zwan, B. J., and R. A. Wolf (1976), Depletion of solar wind plasma near a planetary boundary, *J. Geophys. Res.*, *81*(10), 1636–1648, doi:10.1029/JA081i010p01636.